

Machine learning using structural representations for discovery of high temperature superconductors

Lazar Novakovic,^{1,2} Ashkan Salamat,^{1,2,*} and Keith V. Lawler^{2,†}

¹*Department of Physics & Astronomy, University of Nevada, Las Vegas, Las Vegas, Nevada 89154, USA*

²*Nevada Extreme Conditions Laboratory, University of Nevada, Las Vegas, Las Vegas, NV 89154, USA*

(Dated: January 26, 2023)

The expansiveness of compositional phase space is too vast to fully search using current theoretical tools for many emergent problems in condensed matter physics. The reliance on a deep chemical understanding is one method to identify local minima of relevance to investigate further, minimizing sample space. Utilizing machine learning methods can permit a deeper appreciation of correlations in higher order parameter space and be trained to behave as a predictive tool in the exploration of new materials. We have applied this approach in our search for new high temperature superconductors by incorporating models which can differentiate structural polymorphisms, in a pressure landscape, a critical component for understanding high temperature superconductivity. Our development of a representation for machine learning superconductivity with structural properties allows fast predictions of superconducting transition temperatures (T_c) providing a r^2 above 0.94.

I. INTRODUCTION

Modern exploratory syntheses require extensive assistance from a wide range of computational tools at every step. In the search for high temperature superconductors, a race has been roused with the discovery of hydrogen rich materials under high pressures exhibiting superconducting transitions approaching room temperature.^{1,2} Approaches like crystal structure prediction (CSP) which evaluate the possible stable polymorphs and compositions of a system have been crucial in interpreting the results of solid-state synthesis efforts and compression experiments.³⁻⁷ For superconducting systems, there is the further requirement beyond just stability of calculating the critical superconducting transition temperature (T_c) of a material which can be done ab initio with knowledge only of the material's lattice and atomic configuration.⁸⁻¹¹ These approaches have been taken to identify almost all the known high- T_c superconducting binary hydrides such as H_3S ¹², LaH_{10} ¹³⁻¹⁵, YH_9 ¹⁴, CaH_6 ¹⁶, along with several others.

Ab initio T_c calculations can take on the order of days to months to complete depending on the atomistic complexity and the importance of anharmonicity to the material.¹⁷ Such calculations can be not only long, but also fragile to the assumptions necessary for good accuracy such as the density functional or screened Coulomb interaction.^{18,19} Likewise, recent observations of ternary and higher composition hydrides indicate a more tuneable pathway to achieving ambient conditions superconductivity,^{20,21} but these more complex compositions beyond metal binaries demand significantly more computational efforts to computationally discover new materials.^{1,19,22-24} Because of these complications, there is a strong motivation to develop machine learning methods to rapidly and accurately predict a material's superconducting properties. This has been aided by the decades of superconductivity research and exper-

imental data including Supercon database²⁵, with over 30,000 superconductor measurements of T_c and the corresponding chemical composition (ie stoichiometry).

Stoichiometric derived machine learning models for a superconductor's T_c exist and use additional descriptors such as atomic mass, charge, number of atoms, and similar properties to yield good regression performance.^{26,27} Yet, these models do not include any detail on the 3-dimensionality of the structure as would be needed for ab initio calculations, and thus fail to appreciate details such as the known evolution of the "superconducting dome" of T_c as a function of pressure which arises from the structural changes of a material upon compression. Consequently, difficulties arise when attempting to use data for materials which have a wide range of T_c s measured for several pressures when training these stoichiometric derived models. For instance, recorded T_c s for specific compositions with high variances are often thrown out in these models.^{26,27}

Recently, a new machine learning model predicting superconducting T_c s which includes a description of the 3-dimensional atomic structure has been developed. This model utilizes the smooth overlap of atomic positions (SOAP)²⁸⁻³² descriptors, which incorporates information about the local distributions of positions of atoms around each atom within the structure and has shown improved performance compared to composition models.³³ While the incorporation of the SOAP descriptors provides much needed structural information, the description of local atomic distributions with a cut-off radius could overlook potential similarities between polymorphs within certain values of the cutoff radius as well as neglecting any properties that arise from the full periodic structure of the material such as the phonon dispersion.³⁴

Establishing descriptors capable of accurately capturing structure such as the atomic positions and lattice which affect superconducting properties is thus of tantamount importance for advancing these machine learn-

ing models. Arrangement of periodic atoms should be quantified in a normalized manner for all crystal structures while being weakly dependent on physically invariant transformations such as swapping labels of atoms of identical species or supercells. Here we develop a representation of structural properties for use with machine learning models which boosts predictive precision and extends capabilities for discovery. This representation differentiates polymorphisms and provides physical interpretability of the structural properties. These new descriptors go beyond the SOAP model’s distance based description of the local structure of the material and incorporates the more nuanced properties of the periodic mass and charge distribution of the material. Using the model’s fast prediction speed, we study change in T_c with lattice and atomic species variations of predicted superconducting materials.

II. DATA

A. Supercon

The supercon database contains several thousands of various reported superconducting critical temperatures T_c along with the superconductor’s chemical compositions and the respective experimental paper(s).²⁵ This data needed to be cleaned due to ambiguities and errors, and we chose to use the cleaned version of this data that used in a previous chemical composition machine learning model.²⁶ The data was reformatted by first grouping the sets of T_c s for distinct compositions as is illustrated in Table I. Averages and variances of the T_c s for a given composition were taken to compare the similarity of measured T_c s. Compositions with multiple reported temperatures were delineated into two sets by a cutoff, $\sigma_{T_{cut}}^2$. This demarcation helps determine when temperature averages can accurately represent each set of structures; choosing the cutoff $\sigma_{T_{cut}}^2 = 2$ results in the set $\sigma_{T(y)}^2 < \sigma_{T_{cut}}^2$ having averaged measured T_c s within a few Kelvin. Here, y and $T(y)$ represent the composition and T_c measurements respectively.

B. Materials Project

To add structural information to the T_c values harvested from the Supercon dataset, the compositions from the Supercon data are matched with the corresponding structures on the Materials Project database^{35,36} with the pymatgen library.³⁷ We found 2454 Materials Project structures corresponding with the Supercon compositions, denoted by $S(y)$. For the compositions with a low variance, $\sigma_{T(y)}^2 < \sigma_{T_{cut}}^2$, the gathered T_c values were averaged and that T_c was assigned to the corresponding Materials Project structure. The high

Superconductor	T_c s (K)	$\langle T_c \rangle$ (K)	σ^2 (K ²)
BaLa ₉ (CuO ₄) ₅	29.0, 28.0, ...	24.4	57.1
BaLa ₁₉ Cu ₉ AgO ₄₀	26.0, 27.0	26.5	0.25
BaLa ₁₉ (CuO ₄) ₁₀	19.0, 26.9, ...	28.2	31.9
Ba ₃ La ₃₇ (CuO ₄) ₂₀	22.0, 30.0, ...	27.0	94.3
Ba ₃ La ₁₇ (CuO ₄) ₁₀	23.0, 9.7, ...	16.2	29.5
⋮	⋮	⋮	⋮
CeBiS ₂ O	1.6, 3.0	2.3	0.49
TiSiIr	1.42, 1.85, ...	2.23	0.75
Tm ₂₁ Lu ₄ (Fe ₃ Si ₅) ₂₅	2.44	2.44	0.00
Nb ₄ Pd	1.98	1.98	0.00
Nb ₆₉ Pd ₃₁	1.84	1.84	0.00

TABLE I: Compositions and T_c s for superconductors of the supercon dataset. $\langle T_c \rangle$ denotes the average of T_c s for the superconductor and σ^2 is the variance of the compositions T_c s.

variance compositions with $\sigma_{T(y)}^2 \geq \sigma_{T_{cut}}^2$ (which represents less than 10% of the data) could be treated with at least two different approaches.

Firstly, this data could be excluded because of the impreciseness with setting the mean to structures which allows for more consistent model accuracy. Alternatively, the structures can be labelled with measurements in the respective T_c set that produce the model with the best performance on the validation set. Using a Bayesian process to determine the labelling of high variance data would be helpful to achieve this. Although both of these approaches lead to models with better performance on the validation set, averaging this data is the method with the least data fitting. For this analysis, we chose the third option of averaging this data to study baseline performance.

C. Theoretical Structures

As one of the current motivations for machine learned T_c models is the *a priori* prediction of high pressure hydrogen-based superconductors, theoretical materials that fall into this category but are not within the Supercon dataset were included in our dataset. As these materials are found at higher pressures, there is an associated superconducting dome wherein the T_c varies with pressure. Related, there is also a large degree of potentially accessible compositions and polymorphs within the pressure ranges that are studied experimentally for these materials. 46 high temperature theoretical hydride superconductors of various phases have been introduced into the data set for modelling.¹ The T_c s are labelled by the average of the μ^* bounds used when the T_c was computed through directly solving the Eliashberg equations.

Consequently, this also encodes physical characteristics of the atoms in the field representation. Mass and outer atomic radii are key quantities for prediction in other composition based machine learned superconductivity models.²⁷

Introducing cell periodicity makes the density independent of unit cell choice, however expands the domain beyond a finite region. The fully periodic density is the sum over all cells

$$\Psi_{Z,\Gamma}(\vec{R}; \vec{R}_0) = \sum_{tuv=-\infty}^{\infty} \frac{N_{Z,\Gamma}}{(\sqrt{2\pi}\sigma_{Z,\Gamma})^3} e^{-\frac{(\vec{R}-\vec{R}_0-\vec{\Delta}_{tuv})^2}{2\sigma_{Z,\Gamma}^2}} \quad (5)$$

$$\vec{\Delta}_{tuv} = ta\hat{a} + ub\hat{b} + vc\hat{c}. \quad (6)$$

This is just a convolution of Dirac comb (Eq 7) and the unit cell density (Eq 2)

$$\text{III}_{\vec{\Delta}} = \sum_{tuv=-\infty}^{\infty} \delta^3(\vec{R} - \vec{\Delta}_{tuv}) \quad (7)$$

$$\Psi_{Z,\Gamma}(\vec{R}; \vec{R}_0) = (\psi_{Z,\Gamma}(\vec{R}_0) * \text{III}_{\vec{\Delta}})(\vec{R}). \quad (8)$$

With the periodic field density, the field may be expressed succinctly with far fewer terms through coefficients in

$$\Psi_{Z,\Gamma}(\vec{R}; \vec{R}_0) = \sum_{hkl} \mathcal{F}_{Z,\Gamma}(\vec{h}) e^{i\vec{h} \cdot \vec{R}}. \quad (9)$$

Using shorthand \vec{h} with components h, k , and l , and \vec{h} with the components $\vec{h}_i = 2\pi\vec{h}_i/|\vec{v}_i|$. Eqs 5 and 8 permit obtaining \mathcal{F} by the Poisson summation formula as

$$\mathcal{F}_{Z,\Gamma}(\vec{h}; \vec{R}_0) = \frac{1}{V} F\{\psi_{Z,\Gamma}\} \left(\frac{h}{a}, \frac{k}{b}, \frac{l}{c}; \vec{R}_0 \right). \quad (10)$$

Using cartesian coordinates, with lattice vectors \mathcal{V} , the analogous expression yields

$$\mathcal{F}_{Z,\Gamma} = \frac{1}{V} F\{\psi_{Z,\Gamma}\}(\mathcal{V}^{-1} \cdot \vec{h}). \quad (11)$$

$F\{\psi_{Z,\Gamma}\}$ being the Fourier transform of the original density and h, k, l as integer values

$$\begin{aligned} F\{\psi_{Z,\Gamma}\} &= \iiint_{\mathbb{R}^3} d^3R \psi_{Z,\Gamma}(\vec{R}; \vec{R}_0) e^{-2\pi i \vec{h} \cdot \vec{R}} \\ &= N_{Z,\Gamma} e^{-2\pi^2 \sigma_{Z,\Gamma}^2 \vec{h}^2} e^{-2\pi i \vec{h} \cdot \vec{R}_0}. \end{aligned} \quad (12)$$

Coefficients are therefore given by

$$\mathcal{F}_{Z,\Gamma}(\vec{h}; \vec{R}_0) = \frac{N_{Z,\Gamma}}{V} e^{-\frac{1}{2} \sigma_{Z,\Gamma}^2 \vec{h}^2} e^{-i\vec{h} \cdot \vec{R}_0}. \quad (13)$$

The field can similarly have a periodic localized representation by the von Mises distribution which has periodicity built in and is similar in form to a Gaussian.

$$\Psi_{Z,\Gamma}^{vm}(\vec{R}; \vec{R}_0) = \frac{N_{Z,\Gamma}}{I_0^3(\kappa_{Z,\Gamma})} \prod_j e^{\kappa_{Z,\Gamma} \cos\left(\frac{2\pi}{|\vec{v}_j|} (R_j - R_{0j})\right)} \quad (14)$$

$I_0(\kappa_Z)$ being the modified Bessel function of the first kind and $\kappa_Z \propto \frac{1}{\sigma_Z^2}$.

The Fourier coefficients are given by the modified Bessel functions of the first kind.

$$\mathcal{F}_Z^{vm}(\vec{h}; \vec{R}_0) = \frac{N_Z}{V I_0^3(\kappa_Z)} I_{\vec{h}}(\kappa_Z) I_{\vec{k}}(\kappa_Z) I_{\vec{l}}(\kappa_Z) e^{-i\vec{h} \cdot \vec{R}_0} \quad (15)$$

$I_{\vec{h}}(\kappa_Z)$ increases with κ_Z , meaning the ratios will tend to be of large values. In the region of $\kappa_Z \gg \vec{h}$ this ratio goes to

$$\frac{I_{\vec{h}}(\kappa_Z)}{I_0(\kappa_Z)} \rightarrow e^{-\frac{1}{2\kappa_Z} \vec{h}^2} \quad (16)$$

This shows the similar shape and values of the densities, as expected.

The resulting fields make the input for the spatial data.

$$\mathcal{F}_Z = \mathcal{F}_{Z,e(Z)} \otimes \mathcal{F}_{Z,m(Z)} \quad (17)$$

The coefficients for the entire structure are then the sum of the each atomic contribution of \mathcal{F} by linearity, and the inverse uniquely recreates the density field.

This representation transforms positions of atoms in a lattice to two 3d grids of complex coefficients.

$$\mathbb{F}_{\gamma} : \mathbb{A} \times \mathbb{V} \rightarrow (\mathbb{C} \otimes \mathbb{C})^{\mathbb{Z}^3} \quad (18)$$

An atom in a lattice, $\tilde{\mathcal{A}} \in \mathbb{A} \times \mathbb{V}$, represents each parameter needed in generating the coefficients of the densities, $Z = \pi_1(\tilde{\mathcal{A}})$, $\vec{R}_0 = \pi_2(\tilde{\mathcal{A}})$, $\mathcal{V} = \pi_3(\tilde{\mathcal{A}})$.

$$\mathbb{F}_{\gamma}(\tilde{\mathcal{A}}) = \mathcal{F}_Z(\vec{h}; \vec{R}_0) \quad (19)$$

The Fourier coefficients of the total structure \mathcal{S} is by summing for each atom.

$$\mathcal{F}_{\mathcal{S}} = \sum_{\tilde{\mathcal{A}} \in \mathcal{S}} \mathbb{F}_{\gamma}(\tilde{\mathcal{A}}) \quad (20)$$

Some coefficients are redundant as equation 13 is symmetric for many points and is hermitian. Taking some subset of the coefficients approximates and reduces the data significantly. Reducing by cutting off the coefficients to $0 \leq h, k, l < \delta$ yields a $\delta \times \delta \times \delta \times 2$ set of spatial data to represent the structure.

B. Categorical and Numerical

There are more parameters which are useful to characterize the superconductors beyond the structural properties of atomic densities in a unit cell. In total 175 numerical descriptors were used for this data. Categorical and numerical data consisted of the number of each species in the unit cell up to $N = 86$, 81 chemical descriptors utilized in previous composition model²⁶, along with the 8 descriptors with the lattice parameters and angles, space group number, and volume found using pymatgen.³⁷

IV. MODEL

A. Input and Parameters

The processing parameters necessary for the structural ensemble are: cutoff δ , scaling factors γ_e and γ_m , and \mathcal{F} type and domain.

The form of the descriptors is 3d spatial data having 2 channels which can be modelled through a convolutional neural network (CNN).³⁸ Conventional neural networks are real-valued, however the output of the density is generally complex meaning the input for the convolutional layer will be complex. A complex-valued convolutional neural network (CVCNN) may be appropriate for properly modelling. The data may be made to be real-valued by taking the modulus, real, or imaginary components. This allows use of standard 3d convolutional neural networks although decreases the information of the structure. The data can be treated with a single channel with all the complex data included or with separate channels for each real and imaginary part keep that retain the complete information at a cost of double the data size and connection between the terms. Each of these seemed to work properly relative to each other, though a CVCNN with the cvnn library³⁹ showed the best performance generally.

Various choice of model parameters were used and checked. For this work we chose $\delta = 13$, $\gamma_{e,m} = \{0.0025, 0.25\}$, and $0 \leq h, k, l$ for the processing. Optimal values can be finely tuned, though many configurations, including the chosen parameters, successfully yielded accurate models with novel behavior. The output was taken to be the exact complex values therefore a complex neural network was used. This corresponded to $13 \times 13 \times 13 \times 2$ complex data in the convolution port of the network.

B. Architecture

The model comprises of two input layers with a convolutional layer for spatial density data and a dense neuron layer for the numerical data expressed by figure 2. TensorFlow is used as well as the cvnn package³⁹

for the convolutional layers for building model. Keras tuner was used to tune the number of layers, neurons per layer, and loss function.^{40,41} The numerical data is 4 fully connected 256 unit layers. Spatial data is taken through 2 convolutional layers consisting of 32 units of $3 \times 3 \times 3$ kernels. $2 \times 2 \times 2$ average pooling and 50 percent dropout is used between the layers. A cartesian ReLu activation function is used for the first layer.⁴⁰ The second layer uses an absolute value activation function to convert to real-valued output. This is flattened and then concatenated with the numerical data output layer which follow to 4 fully connected ReLu layers with 512 units and 50 % dropout and a final single neuron output matching output T_c .⁴⁰

In training, a train-test split of 80-20 was used. Many loss functions have been tested in order to best fit the data which includes both several T_c s less than 1 K and above 100 K. The keras Huber loss function with delta=7 was used to prevent outlier data from dominating the error.⁴⁰ The best validation loss model is picked from 300 epochs of training.

V. RESULTS

A. Validation

The model yielded a $r^2 = 0.9429$ with the validation set which shows great performance over the entire prediction space expressed in figure 3. This is without exclusion of any data with high T_c variances. Exclusion of these along with optimizing model architecture and processing of the structure would likely boost the performance as well minimize the number of outliers. Increasing data on T_c s of polymorphisms should also refine the model accuracy, considering the potential number of missing structures which are phases of the superconductors used in the data.

This model provides successful predictions in several studied high temperature superconductors as seen in Table II. In general, this study's model predictions are in much better agreement than the composition-based model²⁶ predictions (Table II) which are unable to predict high T_c structures within the pressure structure landscape. In particular, we were interested in how well this model could predict the superconducting properties of high pressure hydride materials, so structures for materials such as C-S-H, LaH_x, and YH_x were taken from recently published studies.^{1,13,18,19,43,44} Prediction for several of the hydrides are within good agreement of experiment such as a 237 K T_c prediction for P6₃/mmc YH₉ at 255 GPa that has a measured T_c of 237 K.¹⁴ The predicted T_c for LaH₁₀ Fm $\bar{3}$ m at 150 GPa pressure is also close to the measured value of 249 K.¹³ A majority of the computed phases such as LaH₁₀, YH₁₀, and CSH₇ at pressures above 250 GPa are in strong agreement to the calculated T_c s through electron-phonon density functional theory (DFT) calculations.¹⁹ Recently we pub-

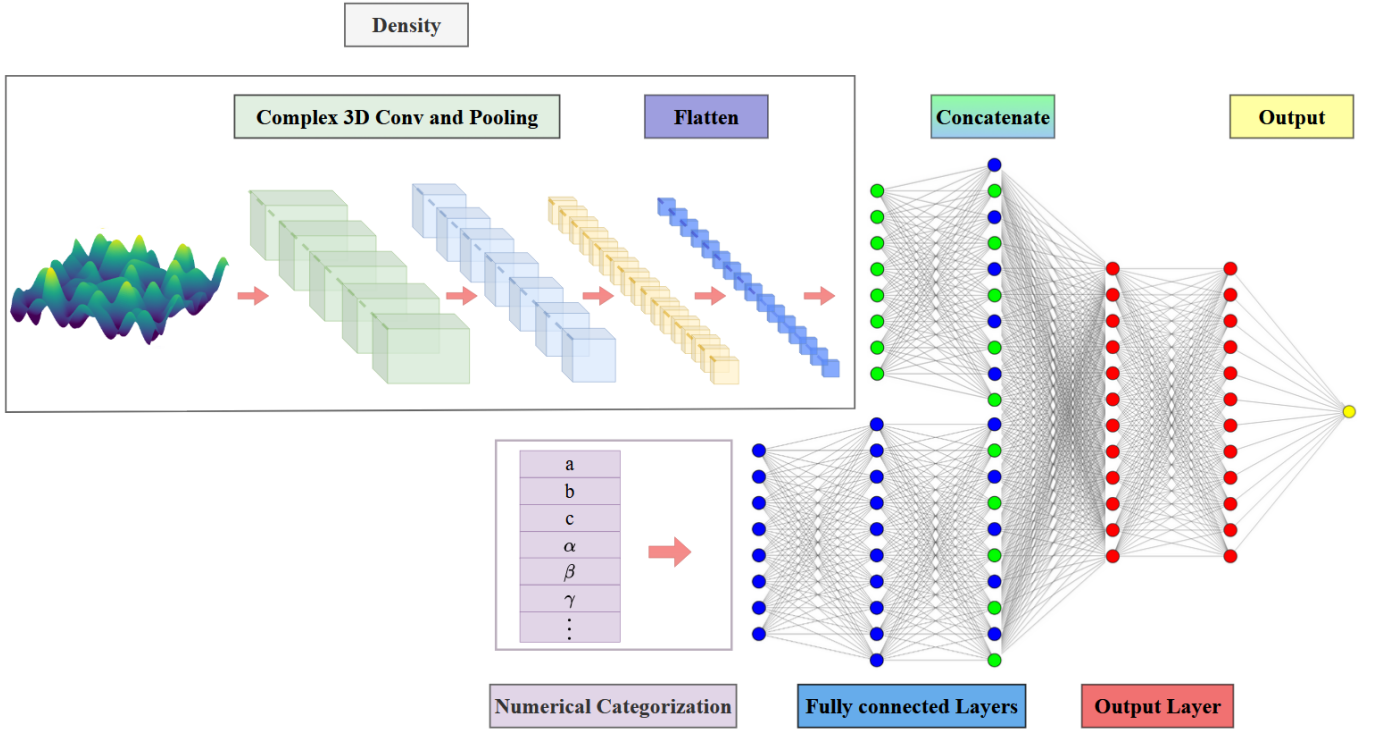


FIG. 2: The architecture of the model. The density information goes through a complex convolution process then flattened. Categorical and numerical data goes to a fully connected layer and is concatenated with the density output.

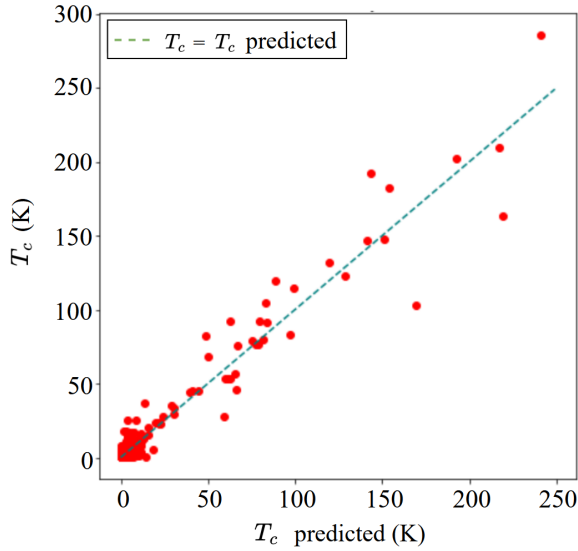


FIG. 3: T_c labelled vs. T_c predicted by the model in the testing set. Where the values equal is expressed by the dashed green line. The r^2 is 0.9429.

lished an investigation into the dependence of the chosen density functional on the calculated T_c for the predicted CSH₇ superconductor at 270 GPa.¹⁸ It was found there that the vdW corrections to the density functional boosted the estimated T_c of a predicted CSH₇ poly-

morph from 80 K to 174 K, which closely follows the model calculated value of 177 K. These are in comparison to the chemical composition predicted values which did not predict above 37 K and cannot distinguish different pressures and phases by the nature of their description. The LiMgH superconductors are not as near to the predicted values though these are the considered an extreme boundary of predicting with electron-phonon calculations as theory is expected to be less reliable for calculation for high temperatures and strong electron-phonon coupling. They are likely more difficult to evaluate through the same system given their T_c s are a large outlier in comparison to those of superconductors used in the training data.

B. Morphisms and Discovery

With large systems electron-phonon calculations may take several weeks for accurate T_c s through Migdal-Eliashberg theory, which can be estimated quickly by the model. Given the depth and quickness of the model, it can facilitate the discovery of candidate high temperature superconductors with diverse and complex structures.

Sets of theoretical superconductors generated through morphisms of base structures through varying the crystal lattice and swapping atomic species

Superconductor	T_c (K) pred	T_c (K) chem	T_c (K)
LaH ₁₀ C2/m (250 GPa)	217	22	215 ¹⁹
YH ₁₀ R $\bar{3}$ m (400 GPa)	268	16	265 ¹⁹
LaH ₁₀ Fm $\bar{3}$ m (250 GPa)	241	21	246 ¹⁹
YH ₁₀ Fm $\bar{3}$ m (400 GPa)	263	16	265 ¹⁹
LaH ₁₀ R $\bar{3}$ m (250 GPa)	236	21	245 ¹⁹
SeH ₃ Im $\bar{3}$ m (200 GPa)	111	28	110 ⁴²
CSH ₅ Cm (150 GPa)	109	37	103 ⁴³
CSH ₇ Pnma (200 GPa)	105	36	129 ⁴³
CSH ₇ R3m (270 GPa)	177	36	174 ^{18*}
CSH ₇ I43m (270 GPa)	162	36	159 ^{18*}
CSH ₇ CmCm (200 GPa)	123	36	-43
CSH ₇ P4m2 (200 GPa)	155	36	-43
CSH ₇ P3m1 (200 GPa)	188	36	-43
CSH ₇ P43m (200 GPa)	191	36	-43
LaH ₁₀ Fm $\bar{3}$ m (150 GPa)	235	36	249 ¹³
YH ₄ I4mmm (167 GPa)	44	21	82 ⁴⁴
YH ₆ Im $\bar{3}$ m (201 GPa)	174	25	211 ¹⁴
YH ₉ P6 ₃ /mmc (255 GPa)	237	14	237 ¹⁴
Li ₂ MgH ₁₆ P $\bar{3}$ m1 (300 GPa)	277	30	191 ²²
Li ₂ MgH ₁₆ Fd $\bar{3}$ m (250 GPa)	293	30	452 ²²
Li ₂ MgH ₁₆ Fd $\bar{3}$ m (300 GPa)	295	30	315 ²²
Li ₂ MgH ₁₆ P1 (300 GPa)	185	30	-22
Li ₂ MgH ₁₆ α -P-1 (300 GPa)	154	30	-22
Li ₂ MgH ₁₆ Pm (300 GPa)	183	30	-22
Li ₂ MgH ₁₆ Cm (300 GPa)	188	30	-22
Li ₂ MgH ₁₆ C2/m (300 GPa)	187	30	-22
Li ₂ MgH ₁₆ Cmc2 (300 GPa)	173	30	-22
Li ₂ MgH ₁₆ I4 (300 GPa)	200	30	-22
Li ₂ MgH ₁₆ R32 (300 GPa)	259	30	-22
LiMgH ₁₀ R $\bar{3}$ m (300 GPa)	267	30	-22
LiMgH ₁₄ Cc (300 GPa)	147	32	-22

TABLE II: Several high temperature superconductors and their predicted T_c s through various methods. T_c pred is this model's prediction, and T_c chem is the chemical type model prediction.²⁶ The final column is the T_c by previous computations or experiments if available. For calculated T_c s the average value of the presented μ^* domain is used. * The calculation is reproduced for this work using the approach of reference¹⁸ and an adjusted 0.015 Ry Gaussian smearing width.

efficiently allows quickly probing an extensive compositional space of diverse superconductors.

Using a system with a low number of atoms as a base is preferable for generating simple structures which are more realistic for measurement and calculation via conventional density functional theory (DFT) approaches, while large systems allows exploration of more complicated landscapes of theoretical high T_c materials where conventional DFT approaches could be cost prohibitive. Im $\bar{3}$ m H₃S at 200 GPa is used as the starting point for the smaller systems because of its simple composition and predicted ~ 200 K T_c ⁴⁵ near the experimental value of 203 K.¹² Whereas Fm $\bar{3}$ m MgH₁₃ supplies a rich space

of variants of larger systems to explore owing to its close to 300 K predicted T_c ¹ as well as its hydrogen-dense composition alike closely studied high T_c superconductors such as LaH₁₀.

Figure 4 shows T_c map for Fm $\bar{3}$ m MgH₁₃ (200 GPa) with the Mg and H^{1,46} each morphed to atoms X and Y, with atomic numbers between 1 to 86. For every generated structure, the lattice parameters were scaled uniformly to determine the respective predicted peak T_c . From this process Fm $\bar{3}$ m LiMgH₁₂ and AlH₁₃ were among the highest suggested superconductors through this discovery method with maximum predicted T_c s of 356 K and 353 K from Table III. LiMgH₁₂ falls among a family of theoretically studied Li_xMgH_y superconductors, many reported to have very high T_c s. Most notably from that study is Fd $\bar{3}$ m Li₂MgH₁₆ which is predicted to have a T_c up to 473 K.²²

For the sulphur-exchanged variations of H₃S, lattices were kept at the original lattice parameters to maintain an idea of the general pressure range. The sulfur-exchanged variants of H₃S place Im $\bar{3}$ m PH₃, BH₃, SeH₃ in the pool of potential high T_c superconductors with T_c s of 191 K, 140 K, and 113 K. These results compare quite well to studied superconductors with Pbcn BH₃ predicted to have a T_c of 125 K at 360 GPa⁴⁷ and a 200 GPa undetermined phase of PH₃ having a measured T_c above 100 K.⁴⁸ Remarkably, the same Im $\bar{3}$ m SeH₃ structure has been estimated through DFT-based approaches to have a nearly identical T_c as what was predicted here, ie. 110 K at 200 GPa.⁴² Following that favorable comparison, our Im $\bar{3}$ m SeH₃ structure was optimized with Quantum Espresso^{49,50} at 200 GPa using the respective vdW-DF2 optimization procedure as detailed in our recent work.¹⁸ This updated the predicted T_c to 111 K from 113 K.

Following the encouraging results on LiMgH₁₂ result, the predicted 250 GPa Fd $\bar{3}$ m Li₂MgH₁₆ material²², 2 formula units in the cell, was used as a base for generating morphisms. Base stoichiometry of the material is therefore Li₄Mg₂H₃₂. Given the high number of atoms, the space for discovery was limited to studying interchanging the Li and Mg atoms. The entire space of 6 atom variations is on the order of $86^6 \approx 10^{12}$ variations without symmetry. This number is completely intractable for first principles evaluations, and it still requires preliminary probing and use of further constraints with the model presented here. A shallow random search explored thousands of morphisms in this space, with magnesium atoms and pairs of lithium atoms replaced with random species of atomic number between 1 and 86. This revealed BaH₃₂N₅ and LaH₃₂N₅, as well as BaH₃₂N₄O and LaH₃₂N₄O variants, well above others in the random probing as potential high temperature superconductors with $T_c > 350$ K as shown in Table III. The number of atoms are fixed using this process and it is possible that by modification, likely the hydrogen density, a lower atom content structure possessing a very high T_c may be generated through

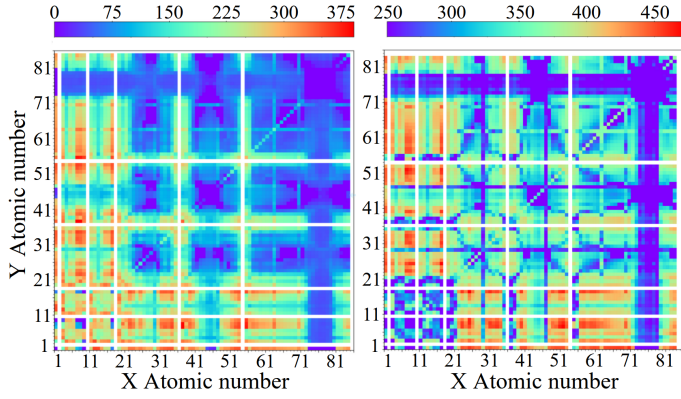


FIG. 4: (left) T_c of $Fm\bar{3}m$ MgH_{13} morphisms with X representing elements swapped with the magnesium atom and Y representing elements swapped with the center hydrogen atom. (right) T_c of $Fd\bar{3}m$ Li_2MgH_{16} morphisms. Here the Li atoms are set to H and the Mg atoms are varied. Atoms with $Z=1$ to 86 are used, and combinations with inert elements (He, Ne, etc.) are expressed by white lines as T_c is not predicted. A T_c vs lattice scale a dome is calculated and the peak T_c is presented here. The initial parameters for the primitive rhombohedral unit cells of $Fm\bar{3}m$ MgH_{13} and $Fd\bar{3}m$ Li_2MgH_{16} are $a = 3.469(5)$ Å and $a = 4.750(7)$ Å respectively.^{1,22}

these.

Hydrogen content replacing lithium atoms showed a higher frequency of high T_c superconductors in the previous example, and it encouraged replacing the Li_4 of the $Li_4Mg_2H_{32}$ to H_4 and investigating morphisms of the form XYH_{36} , ie. only interchanging the magnesium atoms. Figure 4 shows the map of T_c for $Fd\bar{3}m$ XYH_{32} with all atomic pairs between atomic number 1 and 86. This morphism yields several potential room temperature superconductors with T_c well above 400 K such as $LiLaH_{36}$, $ZrH_{36}Cl$, and $TeH_{36}N$ as noted in Table III. The composition model does not capture any of these potential superconductors. Interestingly, the T_c s are predicted to remain high above 200 K even for the very wide scale of the lattice size, implying that lower pressure structures potentially conserve high T_c superconductivity.

C. Physical Aspects

Within the approximation that a material is isomorphic as a function of pressure, varying the lattice parameters over a large range effectively probes the pressure dependent "superconducting dome" of a candidate superconductor. Remarkably, uniformly scaling the lattice of the structures in the data set reveals a superconducting dome similar to T_c versus pressure effects observed experimentally.^{13,51} Polymorphisms had distinct T_c responses to uniform scaling of lattice vectors.

Superconductor	T_c pred (K)	T_c chem (K)
$LiMgH_{12}$ $Fm\bar{3}m$	356 - 213	34
AlH_{13} $Fm\bar{3}m$	353 - 249	47
MnH_{13} $Fm\bar{3}m$	327 - 231	25
$BaH_{32}N_5$ $Fd\bar{3}m$	385 - 302	42
$LaH_{32}N_5$ $Fd\bar{3}m$	434 - 318	41
$BaH_{32}N_4O$ $Fd\bar{3}m$	351 - 234	39
$LaH_{32}N_4O$ $Fd\bar{3}m$	384 - 254	38
$TlBH_{36}$ $Fd\bar{3}m$	403 - 282	26
TlH_{37} $Fd\bar{3}m$	432 - 291	38
LuH_{18} $Fd\bar{3}m$	362 - 243	31
$LiLaH_{36}$ $Fd\bar{3}m$	430 - 316	30
$ZrH_{36}Cl$ $Fd\bar{3}m$	457 - 332	41
$TeH_{36}N$ $Fd\bar{3}m$	471 - 355	46
PH_3 $Im\bar{3}m$	191	64
BH_3 $Im\bar{3}m$	140	59
SeH_3 $Im\bar{3}m$	113	28

TABLE III: Estimated model T_c s of $Fm\bar{3}m$ XYH_{12} (MgH_{13}), $Fd\bar{3}m$ XYH_{36} (Li_2MgH_{16}), and $Im\bar{3}m$ XH_3 (H_3S) morphisms. For XH_3 structures the lattice parameters kept the 200 GPa H_3S primitive rhombohedral lattice values of $a = 2.585$ Å and $\alpha = 109.47^\circ$. For other superconductors the lattice parameters are uniformly scaled to 6.0 Å and the highest and lowest T_c s are expressed. Composition model predictions²⁶ are expressed by column 3, which do not change with structure.

This is demonstrated by figure 5 where $Fd\bar{3}m$ and $P\bar{3}m1$ Li_2MgH_{16} show different volume effects on T_c .

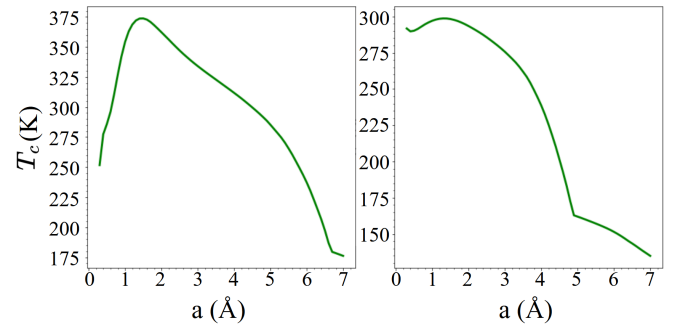


FIG. 5: T_c vs. lattice scaling a for the primitive rhombohedral unit cell of $Fd\bar{3}m$ (left) and $P\bar{3}m1$ (right) Li_2MgH_{16} . Lattice parameters are scaled uniformly with c/a ratios and angles fixed. Initial parameters are $a = 4.750(7)$ Å for the primitive rhombohedral cell of $Fd\bar{3}m$ Li_2MgH_{16} and $a = 2.795(9)$ Å and $c = 5.313(3)$ Å for $P\bar{3}m1$ Li_2MgH_{16} . The initial parameters of $Fd\bar{3}m$ and $P\bar{3}m1$ Li_2MgH_{16} were predicted at 250 and 300 GPa respectively.²²

Varying the lattice parameters $a = b$ and c vs. T_c for the $Fd\bar{3}m$ (in its primitive representation) and $P\bar{3}m1$ structures of Li_2MgH_{12} also exhibits different behavior for the different structures shown in figure 6. The $Fd\bar{3}m$ structure peaks in T_c with equal lattice

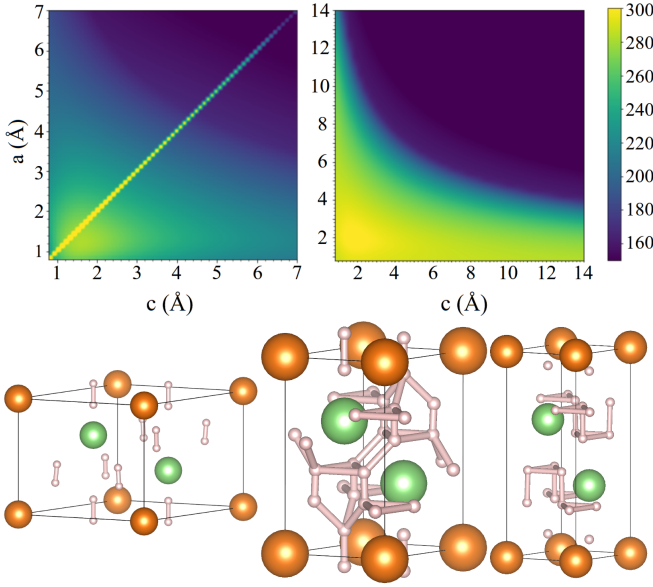


FIG. 6: The predicted T_c for a space of primitive $Fd\bar{3}m$ (upper left) and $P\bar{3}m1$ (upper right) Li_2MgH_{16} lattices. The space spans the lattices with a and c independently varying between 0.8 – 7.0 Å for the $Fd\bar{3}m$ phase and 0.8 – 14.0 Å for the $P\bar{3}m1$ phase. Lattice angles are unchanged and b is constrained by $a = b$ in both cases. Initial parameters are $a = 4.750(7)$ Å for the primitive rhombohedral $Fd\bar{3}m$ cell and $a = 2.795(9)$ Å and $c = 5.313(3)$ Å for $P\bar{3}m1$ (shown bottom center). The $c = 8$ Å (bottom right) and $a = 6$ Å (bottom left) elongations of the initial (bottom center) $P\bar{3}m1$ structure. H–H interaction distances are cut off at 1.4 Å.

lengths (the ideal rhombohedral cell), and T_c drops significantly with asymmetry. The $P\bar{3}m1$ structure on the other hand shows a smooth behavior of the lattice effects on the predicted T_c , with a preference for smaller volumes (ie. higher pressures). The $P\bar{3}m1$ structure shows a rapid drop off in T_c for an expanded $a = b$ -axis, whereas it is more tolerant for deformations of the c -axis. The bottom center structure shown in figure 6 shows the $P\bar{3}m1$ structure with its initial lattice settings of $a = 2.795(9)$ Å and $c = 5.313(3)$ Å, and from this one can see a somewhat 3-dimensional bonding network if the H–H interaction distances are cut off at 1.4 Å — a reasonable distance cutoff for visualizing the clathrate-like H cages in structures such as YH_6 and YH_9 .^{14,44} When the c -axis is stretched (keeping $a = b$ fixed) as shown in the bottom right of figure 6 (with $c = 8$ Å), the H–H interaction networks in the ab planes are not broken. However, keeping c fixed and stretching $a = b$ as shown with $a = 6$ Å in the bottom left of figure 6 disrupts this 2-dimensional connectivity leaving only non-connected, molecular-like H–H units, strongly

implying that the 2-dimensional H–H structural motif is what is driving the T_c predicted by our model.

VI. CONCLUSIONS

Composition models have presented a successful concept for possibilities in machine learning approaches to superconductor research. However, implementing such models for the analysis and discovery of superconductors requires completely encapsulating their identity. Including structural descriptors as is done here enables studying characteristic behavior such as superconducting domes, symmetry, and atomic periodicity which is proving to be critical for the discovery and understanding of superconducting hydride materials at high pressures. The periodic electron and mass densities descriptors were represented with a complex-valued CNN as their smooth densities are naturally complex valued and are analogous to 3d image data for which CNNs are commonly employed. Though chemical composition derived properties are built within this density representation, non-structural parameters are still used because of relevant information such as electronegativity and number of valence electrons, which are not expressed formally by densities of mass and charge.

The structural representation independently suggests studied theoretical superconductors such as aluminum and iodine hydrides as well as $LiMgH_{12}$, results not captured by composition models. The model presented here also provides unique inverses of the atomic structure by the Fourier representation, thus enabling purely T_c based explorations of structural landscapes as highlighted here with the case study on Li_2MgH_{16} . Utilizing a structural based machine learned modelling of T_c along with crystal structure prediction can be used in the future to create a screening procedure that will increase the discovery efficiency of experimentally feasible materials. Especially, as future versions could benefit from more accurate representations of the electron and mass densities derived from CSP. Theoretical and experimental validation of the structures predicted by this model will only increase data availability which can be used to further refine such machine learning approaches.

This work's data and code will be made available at <https://github.com/LazarNov/superconductor-predict>.

VII. ACKNOWLEDGEMENTS

This work supported by the U.S. Department of Energy, Office of Basic Energy Sciences under Award Number DE-SC0020303. Computational resources were provided by the UNLV National Supercomputing Institute.

- * salamat@physics.unlv.edu
† keith.lawler@unlv.edu
- ¹ A. M. Shipley, M. J. Hutcheon, R. J. Needs, and C. J. Pickard, *Physical Review B* **104** (2021), 10.1103/physrevb.104.054501.
 - ² X. Wang, T. Bi, K. Hilleke, A. Lamichhane, R. Hemley, and E. Zurek, *npj Computational Materials* **8** (2022), 10.1038/s41524-022-00769-9.
 - ³ D. C. Lonie and E. Zurek, *Computer Physics Communications* **182**, 372 (2011).
 - ⁴ P. Avery, C. Toher, S. Curtarolo, and E. Zurek, *Computer Physics Communications* **237**, 274 (2019).
 - ⁵ A. O. Lyakhov, A. R. Oganov, H. T. Stokes, and Q. Zhu, *Comp. Phys. Commun.* **184**, 1172 (2013).
 - ⁶ Y. Wang, J. Lv, L. Zhu, and Y. Ma, *Phys. Rev. B* **82**, 094116 (2010).
 - ⁷ C. J. Pickard and R. J. Needs, *Journal of Physics: Condensed Matter* **23**, 053201 (2011).
 - ⁸ M. Wierzbowska, S. de Gironcoli, and P. Giannozzi, “Origins of low- and high-pressure discontinuities of t_c in niobium,” (2005).
 - ⁹ A. M. Shipley, M. J. Hutcheon, M. S. Johnson, R. J. Needs, and C. J. Pickard, *Phys. Rev. B* **101**, 224511 (2020).
 - ¹⁰ F. Giustino, M. L. Cohen, and S. G. Louie, *Phys. Rev. B* **76**, 165108 (2007).
 - ¹¹ S. Ponc  , E. Margine, C. Verdi, and F. Giustino, *Computer Physics Communications* **209**, 116 (2016).
 - ¹² A. P. Drozdov, M. I. Erements, I. A. Troyan, V. Ksenofontov, and S. I. Shylin, *Nature* **525**, 73 (2015).
 - ¹³ A. P. Drozdov, P. P. Kong, V. S. Minkov, S. P. Besedin, M. A. Kuzovnikov, S. Mozaffari, L. Balicas, F. F. Balakirev, D. E. Graf, V. B. Prakapenka, E. Greenberg, D. A. Knyazev, M. Tkacz, and M. I. Erements, *Nature* **569**, 528 (2019).
 - ¹⁴ P. Kong, V. S. Minkov, M. A. Kuzovnikov, A. P. Drozdov, S. P. Besedin, S. Mozaffari, L. Balicas, F. F. Balakirev, V. B. Prakapenka, S. Chariton, D. A. Knyazev, E. Greenberg, and M. I. Erements, *Nature Communications* **12** (2021), 10.1038/s41467-021-25372-2.
 - ¹⁵ M. Somayazulu, M. Ahart, A. K. Mishra, Z. M. Geballe, M. Baldini, Y. Meng, V. V. Struzhkin, and R. J. Hemley, *Phys. Rev. Lett.* **122**, 027001 (2019).
 - ¹⁶ L. Ma, K. Wang, Y. Xie, X. Yang, Y. Wang, M. Zhou, H. Liu, X. Yu, Y. Zhao, H. Wang, G. Liu, and Y. Ma, *Physical Review Letters* **128** (2022), 10.1103/physrevlett.128.167001.
 - ¹⁷ L. Monacelli, R. Bianco, M. Cherubini, M. Calandra, I. Errea, and F. Mauri, *Journal of Physics: Condensed Matter* **33**, 363001 (2021).
 - ¹⁸ L. Novakovic, D. Sayre, D. Schacher, R. P. Dias, A. Salamat, and K. V. Lawler, *Physical Review B* **105** (2022), 10.1103/physrevb.105.024512.
 - ¹⁹ A. M. Shipley, M. J. Hutcheon, M. S. Johnson, R. J. Needs, and C. J. Pickard, *Physical Review B* **101** (2020), 10.1103/physrevb.101.224511.
 - ²⁰ E. Snider, N. Dasenbrock-Gammon, R. McBride, M. Debesai, H. Vindana, K. Vencatasamy, K. V. Lawler, A. Salamat, and R. P. Dias, *Nature* **586**, 373 (2020).
 - ²¹ S. D. Cataldo, C. Heil, W. von der Linden, and L. Boeri, *Physical Review B* **104** (2021), 10.1103/physrevb.104.1020511.
 - ²² Y. Sun, J. Lv, Y. Xie, H. Liu, and Y. Ma, *Physical Review Letters* **123** (2019), 10.1103/physrevlett.123.097001.
 - ²³ L.-L. Liu, H.-J. Sun, C. Z. Wang, and W.-C. Lu, *Journal of Physics: Condensed Matter* **29**, 325401 (2017).
 - ²⁴ H. Liu, I. I. Naumov, R. Hoffmann, N. Ashcroft, and R. J. Hemley, *Proceedings of the National Academy of Sciences* **114**, 6990 (2017).
 - ²⁵ “Supercon database: <https://supercon.nims.go.jp/>,” .
 - ²⁶ K. Hamidieh, (2018), 10.48550/ARXIV.1803.10260.
 - ²⁷ V. Stanev, C. Oses, A. G. Kusne, E. Rodriguez, J. Paglione, S. Curtarolo, and I. Takeuchi, *npj Computational Materials* **4** (2018), 10.1038/s41524-018-0085-8.
 - ²⁸ S. De, A. P. Bart  k, G. Cs  nyi, and M. Ceriotti, *Physical Chemistry Chemical Physics* **18**, 13754 (2016).
 - ²⁹ M. J  ger, E. Morooka, F. Canova, L. Himanen, and A. Foster, *npj Computational Materials* **4** (2018), 10.1038/s41524-018-0096-5.
 - ³⁰ A. P. Bart  k, R. Kondor, and G. Cs  nyi, *Physical Review B* **87** (2013), 10.1103/physrevb.87.184115.
 - ³¹ F. Musil, A. Grisafi, A. P. Bart  k, C. Ortner, G. Cs  nyi, and M. Ceriotti, *Chemical Reviews* **121**, 9759 (2021), pMID: 34310133, <https://doi.org/10.1021/acs.chemrev.1c00021>.
 - ³² J. Townsend, C. P. Micucci, J. H. Hymel, V. Maroulas, and K. D. Vogiatzis, *Nature Communications* **11** (2020), 10.1038/s41467-020-17035-5.
 - ³³ J. Zhang, Z. Zhu, X.-D. Xiang, K. Zhang, S. Huang, C. Zhong, H.-J. Qiu, K. Hu, and X. Lin, *The Journal of Physical Chemistry C* **126**, 8922 (2022), <https://doi.org/10.1021/acs.jpcc.2c01904>.
 - ³⁴ P. B. Allen and B. Mitrovi   (Academic Press, 1983) pp. 1–92.
 - ³⁵ A. Jain, S. P. Ong, G. Hautier, W. Chen, W. D. Richards, S. Dacek, S. Cholia, D. Gunter, D. Skinner, G. Ceder, and K. a. Persson, *APL Materials* **1**, 011002 (2013).
 - ³⁶ S. P. Ong, S. Cholia, A. Jain, M. Brafman, D. Gunter, G. Ceder, and K. A. Persson, *Computational Materials Science* **97**, 209 (2015).
 - ³⁷ S. P. Ong, W. D. Richards, A. Jain, G. Hautier, M. Kocher, S. Cholia, D. Gunter, V. L. Chevrier, K. A. Persson, and G. Ceder, *Computational Materials Science* **68**, 314 (2013).
 - ³⁸ Y. LeCun, Y. Bengio, and G. Hinton, *Nature* **521**, 436 (2015).
 - ³⁹ J. A. Barrachina, “Negu93/cvnn: Complex-valued neural networks,” (2022).
 - ⁴⁰ M. Abadi, A. Agarwal, P. Barham, E. Brevdo, Z. Chen, C. Citro, G. S. Corrado, A. Davis, J. Dean, M. Devin, S. Ghemawat, I. Goodfellow, A. Harp, G. Irving, M. Isard, Y. Jia, R. Jozefowicz, L. Kaiser, M. Kudlur, J. Levenberg, D. Man  , R. Monga, S. Moore, D. Murray, C. Olah, M. Schuster, J. Shlens, B. Steiner, I. Sutskever, K. Talwar, P. Tucker, V. Vanhoucke, V. Vasudevan, F. Vi  gas, O. Vinyals, P. Warden, M. Wattenberg, M. Wicke, Y. Yu, and X. Zheng, “TensorFlow: Large-scale machine learning on heterogeneous systems,” (2015), software available from tensorflow.org.
 - ⁴¹ T. O’Malley, E. Bursztein, J. Long, F. Chollet, H. Jin, L. Invernizzi, *et al.*, “Kerastuner,” <https://github.com/keras-team/keras-tuner> (2019).
 - ⁴² S. Zhang, Y. Wang, J. Zhang, H. Liu, X. Zhong, H.-F. Song, G. Yang, L. Zhang, and Y. Ma, *Scientific reports* **5**, 1 (2015).

- ⁴³ W. Cui, T. Bi, J. Shi, Y. Li, H. Liu, E. Zurek, and R. J. Hemley, *Physical Review B* **101** (2020), 10.1103/physrevb.101.134504.
- ⁴⁴ Y. Wang, K. Wang, Y. Sun, L. Ma, Y. Wang, B. Zou, G. Liu, M. Zhou, and H. Wang, *Chinese Physics B* **31**, 106201 (2022).
- ⁴⁵ M. Borinaga, I. Errea, M. Calandra, F. Mauri, and A. Bergara, *Phys. Rev. B* **93**, 174308 (2016).
- ⁴⁶ Structure files are available by <https://github.com/LazarNov/superconductor-predict>. Atoms labelled as X/Y specify the morphed sites.
- ⁴⁷ K. Abe and N. W. Ashcroft, *Phys. Rev. B* **84**, 104118 (2011).
- ⁴⁸ A. P. Drozdov, M. I. Eremets, and I. A. Troyan, “Superconductivity above 100 k in Pb at high pressures,” (2015).
- ⁴⁹ P. Giannozzi, S. Baroni, N. Bonini, M. Calandra, R. Car, C. Cavazzoni, D. Ceresoli, G. L. Chiarotti, M. Cococcioni, I. Dabo, A. D. Corso, S. de Gironcoli, S. Fabris, G. Fratesi, R. Gebauer, U. Gerstmann, C. Gougoussis, A. Kokalj, M. Lazzeri, L. Martin-Samos, N. Marzari, F. Mauri, R. Mazarello, S. Paolini, A. Pasquarello, L. Paulatto, C. Sbraccia, S. Scandolo, G. Sclauzero, A. P. Seitsonen, A. Smogunov, P. Umari, and R. M. Wentzcovitch, *J. Phys.: Cond. Matter* **21**, 395502 (2009).
- ⁵⁰ P. Giannozzi, O. Andreussi, T. Brumme, O. Bunau, M. B. Nardelli, M. Calandra, R. Car, C. Cavazzoni, D. Ceresoli, M. Cococcioni, N. Colonna, I. Carnimeo, A. D. Corso, S. de Gironcoli, P. Delugas, R. A. DiStasio, A. Ferretti, A. Floris, G. Fratesi, G. Fugallo, R. Gebauer, U. Gerstmann, F. Giustino, T. Gorni, J. Jia, M. Kawamura, H.-Y. Ko, A. Kokalj, E. Küçükbenli, M. Lazzeri, M. Marsili, N. Marzari, F. Mauri, N. L. Nguyen, H.-V. Nguyen, A. O. de-la-Roza and L. Paulatto, S. Poncé, D. Rocca, R. Sabatini, B. Santra, M. Schlipf, A. P. Seitsonen, A. Smogunov, I. Timrov, T. Thonhauser, P. Umari, N. Vast, X. Wu, and S. Baroni, *J. Phys.: Cond. Matter* **29**, 465901 (2017).
- ⁵¹ C. C. Zhu, X. F. Yang, W. Xia, Q. W. Yin, L. S. Wang, C. C. Zhao, D. Z. Dai, C. P. Tu, B. Q. Song, Z. C. Tao, Z. J. Tu, C. S. Gong, H. C. Lei, Y. F. Guo, and S. Y. Li, *Phys. Rev. B* **105**, 094507 (2022).